ASME Journal of Turbomachinery
Online journal at:
https://asmedigitalcollection.asme.org/turbomachinery

Giacomo Pastorino[1]
Turbomachinery and Propulsion Department,
von Karman Institute for Fluid Dynamics,
Rhode Saint Genèse 1640, Belgium;
Département d'Aérospatiale et Mécanique,
Université de Liège,
Liège B-4000, Belgium
e-mail: giacomo.pastorino@vki.ac.be

Loris Simonassi[2]
Turbomachinery and Propulsion Department,
von Karman Institute for Fluid Dynamics,
Rhode Saint Genèse 1640, Belgium
e-mail: loris.simonassi@avioaero.it

Gustavo Lopes
Turbomachinery and Propulsion Department,
von Karman Institute for Fluid Dynamics,
Rhode Saint Genèse 1640, Belgium;
Département d'Aérospatiale et Mécanique,
Université de Liège,
Liège B-4000, Belgium
e-mail: gustavo.lopes@vki.ac.be

Elissavet Boufidi
Turbomachinery and Propulsion Department,
von Karman Institute for Fluid Dynamics,
Rhode Saint Genèse 1640, Belgium
e-mail: elissavet.boufidi@vki.ac.be

Fabrizio Fontaneto
Turbomachinery and Propulsion Department,
von Karman Institute for Fluid Dynamics,
Rhode Saint Genèse 1640, Belgium
e-mail: fontaneto@vki.ac.be

Sergio Lavagnoli
Turbomachinery and Propulsion Department,
von Karman Institute for Fluid Dynamics,
Rhode Saint Genèse 1640, Belgium
e-mail: lavagnoli@vki.ac.be

Measurements of Turbulence in Compressible Low-Density Flows at the Inlet of a Transonic Linear Cascade With and Without Unsteady Wakes

In the present work, hot-wire anemometry was employed for the characterization of the turbulent field at the inlet of a high-speed low-pressure turbine cascade, in terms of turbulence intensity and integral length scales. This work addresses two major topics relevant to the turbomachinery field: the application of hot-wire anemometry in transonic and rarefied flow regimes and the decoupling of the deterministic and the stochastic fluctuations when measuring unsteady phenomena. In compressible and rarefied flows, a hot-wire is strongly sensitive to both density and velocity fluctuations, and the commonly used Nusselt–Reynolds correlations are not valid. In this article, a nondimensional calibration methodology, based on Nusselt, Reynolds, and Knudsen numbers, was coupled with a sensitivity analysis and employed to postprocess the experimental dataset, allowing to decouple the fluctuations of density and velocity and to compute the turbulence parameters. In the presence of unsteady wakes generated upstream of the cascade, two different phase-locked averaging techniques were employed to distinguish the wake deterministic fluctuations from the background turbulence intensity. [DOI: 10.1115/1.4064369]

Keywords: low-pressure turbine, transonic low-density flows, unsteady wakes, turbulence measurements, hot-wire anemometry, hot-wire sensitivity

1 Introduction

Constant temperature hot-wire anemometry (CTA) is among the most common techniques for measuring turbulent velocity fluctuations, thanks to its excellent spatial resolution and frequency response [1]. The CTA technique is based on the forced convective heat transfer between a heated wire, kept at constant temperature by the anemometer control system, and a colder impinging flow [2]. To keep the wire temperature (hence the resistance) constant, the anemometer modulates continuously the current in the circuit, resulting in variations of voltage on the anemometer bridge. Through a proper calibration, the fluctuations of voltage can be related to the velocity fluctuations in the flow, allowing the measurement of turbulence. Despite the simple operating principle and the widely spread usage, robust methodologies for hot-wire applications only exist for incompressible and supersonic flows, and few studies documented the use of thermal anemometry in low-density transonic flows [2]. The present work is focused on the study of turbulence in a transonic low-density environment, at the engine-representative flow conditions of a high-speed low-pressure turbine for geared

[1]Corresponding author.
[2]Present address: Avio Aero, 10040 Rivalta di Torino TO, Italy.

Contributed by of ASME for publication in the Journal of Turbomachinery. Manuscript received October 27, 2023; final manuscript received November 30, 2023; published online February 26, 2024. Tech. Editor: David G. Bogard.

turbofans. In these Mach number regimes ($0.3 \leq M \leq 1$), the hot-wire output voltage E_b is strongly sensitive to velocity, density, and total temperature fluctuations present in the flow:

$$E_b' = f(u', \rho', T_0') \tag{1}$$

Due to this dependency, it is particularly challenging to isolate only the velocity fluctuations u', required to compute turbulence parameters, since large errors can be generated by neglecting the contributions of ρ' and T_0', as highlighted by Boufidi and Fontaneto [3]. As a consequence, in CTA, the calibration and data reduction techniques strongly depend on the flow under investigation, as well as on the number and orientation of the wires.

The most common calibration methodology, the "King's law" [4], directly links the bridge voltage E_b to the flow velocity u. Because of its simplicity, this technique can be applied only in simplified scenarios (isothermal and incompressible flows, and with a wire perpendicular to the stream). A further development of the King's law is the mass flux calibration, linking bridge voltage and the mass flux $\rho \cdot u$, where ρ is the flow density. An application of this calibration approach to low-density compressible flows was reported by Chemnitz and Niehuis [5]. To decouple density from velocity, this approach would need a time series of density fluctuations. The authors, however, exploited the average static density measured by 5-hole pressure probes to retrieve the velocity fluctuations. As a consequence, this method only provides reliable results in the case of negligible density fluctuations ($\rho' \sim 0$).

Alternatively, other authors have employed a nondimensional mass flux calibration, expressed as a function of the wire's Reynolds number Re_w and the Nusselt number Nu [2,3,6,7]. The wire's Reynolds number is calculated as follows:

$$\mathrm{Re}_w = \frac{\rho \cdot u \cdot d_w}{\mu} \tag{2}$$

where μ is the dynamic viscosity and d_w is the wire diameter. The Nusselt number is calculated from the output bridge voltage as follows:

$$\mathrm{Nu} = \frac{E_b^2}{\pi l_w k \left(T_w - \eta T_0\right)} \frac{R_w}{(R_t + R_s + R_w)^2} \tag{3}$$

where R_w, R_s, R_t, l_w, k, η, and T_w are the wire resistance, support resistance, total resistance, effective wire length, thermal conductivity, recovery factor, and effective wire temperature, respectively. In these works, the recovery factor was determined as $\eta = f(\mathrm{Re}_w, M)$ from semi-empirical correlations proposed by Dewey [8]. In incompressible and continuum flows, the Nusselt number is a unique function of the Reynolds number, so $\mathrm{Nu} = f(\mathrm{Re}_w)$ [3,6]. Thus, from a $\mathrm{Nu} - \mathrm{Re}_w$ calibration curve, it is possible to compute Re_w, and if the value of density ρ is known, one can retrieve the velocity fluctuations. In compressible and/or rarefied flow regimes, the Nusselt number is also a function of the wire's Knudsen number Kn [6,9]. The Knudsen number, defined as the ratio of the molecular mean free path length to a characteristic length (the wire diameter in this case), is used to express the deviation from the continuum flow state. Based on its value, three flow regimes can be identified, providing an indication of the degree of rarefaction of the gas: continuum flows for $\mathrm{Kn} < 0.01$, slip flows for $0.01 < \mathrm{Kn} < 0.1$, and transitional to free-molecular flows for $0.1 < \mathrm{Kn} < 10$ [3]. The Knudsen number can also be expressed as a function of M and Re_w [8]:

$$\mathrm{Kn} = \frac{\mathrm{M}}{\mathrm{Re}_w} \cdot \sqrt{\frac{\gamma \pi}{2}} \tag{4}$$

As a consequence, by fixing two parameters among Re_w, M, and Kn, the third one is unequivocally defined. For hot-wire anemometry in compressible flows, the following equations are thus valid:

$$\mathrm{Nu} = f(\mathrm{Re}_w, \mathrm{Kn}); \quad \mathrm{Nu} = f(\mathrm{Re}_w, \mathrm{M}); \quad \mathrm{Nu} = f(\mathrm{Kn}, \mathrm{M}) \tag{5}$$

Examples of nondimensional mass flux calibrations in compressible low-density regimes were presented by Boufidi and Fontaneto [3]: the scattered and discontinuous trends of the calibration points clearly highlighted the dependency of Nu not only on Re_w but also on Kn, i.e., on the Mach number. In Refs. [3,6], to tackle this problem and obtain a continuous curve, sets of semi-empirical correlations proposed by Dewey [8] and Klopfer [10] were exploited. These correlations allowed to obtain a Mach-independent corrected Nusselt number, $\mathrm{Nu}_{\mathrm{corr}}$, solely function of Re_w. Dewey's formulation is given as follows:

$$\mathrm{Nu}_{\mathrm{corr}}\,(\mathrm{Re}_w) = \frac{\mathrm{Nu}(\mathrm{Re}_w, \mathrm{M})}{\phi(\mathrm{Re}_w, \mathrm{M})} \tag{6}$$

The correction term $\phi(\mathrm{Re}_w, \mathrm{M})$ relates the actual Nusselt number to the one that would be obtained for a highly supersonic flow ($\mathrm{Nu}_{\mathrm{corr}}$) that has been found to be Mach-independent. This correlation is valid for $0.3 \leq M \leq 1$. The correlation of Klopfer is an extension down to $M = 0$ of Dewey's equation, valid in the range $0 \leq M \leq 0.4$. In Refs. [3,6], the $\mathrm{Nu}_{\mathrm{corr}} - \mathrm{Re}_w$ approach eliminated the dependency on the Mach number. However, the correction term ϕ is unknown a priori if M and Re_w are unknown. For this reason, Cukurel et al. [6] developed an iterative procedure to compute a time series of Re_w, i.e., $(\rho u)'$. Again, in order to isolate the time series of u', an unknown time series of density fluctuations ρ' would be necessary.

All the calibration approaches presented in this introduction suffer from inaccuracies in compressible and rarefied flow regimes due to the difficulty of decoupling the instantaneous fluctuations of density and velocity and due to the Nusselt number dependency on both Mach and Knudsen numbers. The traditional calibration and data reduction techniques are thus oversimplifying the flow, neglecting the contribution of the density fluctuations, and they often rely on semi-empirical correlations in order to eliminate the Mach and Knudsen numbers dependencies.

2 The Sensitivity Equation

Pioneering studies of Kovasznay [11] and Morkovin [12] laid the foundations for the application of hot-wire anemometry in supersonic and transonic flows, respectively. These methods, valid for small turbulent perturbations, are based on a sensitivity analysis, under the assumption that the hot-wire output depends on velocity, density, and total temperature fluctuations. By performing the logarithmic differentiation of Eq. (1), for a hot-wire perpendicular to the flow, the following equation is derived:

$$\frac{E_b'}{E_b} = S_\rho \cdot \frac{\rho'}{\overline{\rho}} + S_u \cdot \frac{u'}{\overline{u}} + S_{T_0} \cdot \frac{T_0'}{T_0} \tag{7}$$

where S_ρ, S_u, and S_{T_0} are the hot-wire sensitivities to density, velocity, and total temperature, respectively. To the authors knowledge, this is the only equation isolating the simultaneous fluctuations of velocity, density, and total temperature. The sensitivities S_ρ, S_u, and S_{T_0} can be computed experimentally [3] from Eqs. (8)–(10):

$$S_\rho = \left(\frac{\partial \log E_b}{\partial \log \rho}\right)_{T_0, u = \mathrm{const}} \tag{8}$$

$$S_u = \left(\frac{\partial \log E_b}{\partial \log u}\right)_{\rho, T_0 = \mathrm{const}} \tag{9}$$

$$S_{T_0} = \left(\frac{\partial \log E_b}{\partial \log T_0}\right)_{\rho, u = \mathrm{const}} \tag{10}$$

However, this approach would require extremely time-consuming calibrations in closed-loop facilities, methodically varying one parameter while keeping the others constant. These sensitivities can be more conveniently expressed in a nondimensional form, as

a function of Nu, Re_w, M, and recovery factor η [9]:

$$S_\rho = \frac{1}{2}\left(\frac{\partial \log \mathrm{Nu}}{\partial \log \mathrm{Re}_w} + \frac{\partial \log \eta}{\partial \log \mathrm{Re}_w}\right) \tag{11}$$

$$S_u = S_\rho + \frac{1}{2K_1}\left(\frac{\partial \log \mathrm{Nu}}{\partial \log \mathrm{M}} - \frac{1}{\tau_w}\frac{\partial \log \eta}{\partial \log \mathrm{M}}\right) \tag{12}$$

$$S_{T_0} = \frac{1}{2}\left[K_2 + 1 - K_3\frac{\partial \log \mathrm{Nu}}{\partial \log \mathrm{Re}_w} - \frac{\theta-\eta}{\theta} + \frac{1}{\tau_w}\cdot \left(-\frac{1}{2K_1}\frac{\partial \log \eta}{\partial \log \mathrm{M}} + K_3\frac{\partial \log \eta}{\partial \log \mathrm{Re}_w}\right) - \frac{1}{2K_1}\frac{\partial \log \mathrm{Nu}}{\partial \log \mathrm{M}}\right] \tag{13}$$

where $K_1 = [1+\mathrm{M}^2\cdot(\gamma-1)/2]^{-1}$, $K_2 = \partial \log k/\partial \log T_0$, $K_3 = \partial \log \mu/\partial \log T_0$, $\theta = T_w/T_0$ and $\tau_w = (T_w - \eta T_0)/(\eta T_0)$. If a $\mathrm{Nu_{corr}}$–Re_w calibration curve is employed, Boufidi and Fontaneto [3] proposed the following formulations to compute the partial derivatives of Nu with respect to Re_w and M:

$$\frac{\partial \log \mathrm{Nu}}{\partial \log \mathrm{Re}_w} = \frac{\mathrm{Re}_w}{\phi}\frac{\partial \phi}{\partial \mathrm{Re}_w} + \frac{\partial \log \mathrm{Nu_{corr}}}{\partial \log \mathrm{Re}_w} \tag{14}$$

$$\frac{\partial \log \mathrm{Nu}}{\partial \log \mathrm{M}} = \frac{M}{\phi}\frac{\partial \phi}{\partial \mathrm{M}} \tag{15}$$

where ϕ is the Dewey's corrective factor of Eq. (6). Different authors who analyzed the hot-wire response in compressible flows [3,6,9,13] reported that typical values of S_ρ are on the order of 0.2–0.25. By contrast, the values of S_u were found to be scattered, ranging between 0.01 and 0.25. All the authors agreed that S_u is smaller than S_ρ, making extremely challenging to isolate u' in compressible flows. The total temperature sensitivity S_{T_0} was always found to be negative and higher in absolute value compared to S_u and S_ρ. Its value was strongly dependent on the difference between the wire temperature T_w and the flow total temperature T_0, and varied between −0.5 and −1.2 [3]. In Eq. (7), the three fluctuations u', ρ', and T_0' are the unknowns. Multiwire probes can be exploited in order to isolate these unknowns: for a three-wire probe, provided that the sensitivities of each wire are different, a system with three sensitivity equations can be solved, decoupling u', ρ', and T_0'. Yablochkin and Cukurel [14] proposed a guideline for the selection of an optimal multiwire probe, featuring wires with different sensitivities. The authors concluded that, in order to achieve different S_u and S_ρ, wires with different diameters must be selected, while different T_w values are necessary to vary S_{T_0}.

Equation (7) can also be generalized for slanted wire configurations, including two new terms $S_\alpha \cdot \alpha'$ and $S_\beta \cdot \beta'$, where α' and β' are the fluctuations of yaw and pitch angles, respectively. According to Motallebi [15], the angular sensitivity coefficients S_α and S_β can be determined experimentally by systematically varying yaw and pitch angles in a dedicated angular calibration facility. The formulation is expressed in Eqs. (16) and (17):

$$S_\alpha = \frac{1}{2}\left(\frac{1}{\tau_w}\frac{\partial \log \eta}{\partial \alpha} - \frac{\partial \log \mathrm{Nu}}{\partial \alpha}\right) \tag{16}$$

$$S_\beta = \frac{1}{2}\left(\frac{1}{\tau_w}\frac{\partial \log \eta}{\partial \beta} - \frac{\partial \log \mathrm{Nu}}{\partial \beta}\right) \tag{17}$$

Boufidi and Fontaneto [3] observed that the angular sensitivities depend only on the orientation of the wire, not on the overheat ratio or its diameter. In Refs. [6,15], it was concluded that a single angular calibration is representative for every flow condition, since no Reynolds nor Mach number dependencies could be identified. Cukurel et al. [6] performed a study on the angular calibration procedure for a cross-wire probe, featuring two slanted wires, and showed that the time series of the fluctuating yaw angle could be computed before the application of the sensitivity equation through an angular calibration that was independent of the flow conditions. The angular fluctuations α' were found to be a unique function of the ratio of the instantaneous Reynolds numbers of the two wires, previously computed from two $\mathrm{Nu_{corr}}$ – Re_w calibration curves. Consequently, the term $S_\alpha \cdot \alpha'$ was computed and inserted in the left-hand side of Eq. (7).

In this work, the hot-wire sensitivity method was employed in order to decouple the instantaneous fluctuations of density ρ' and velocity u' at the inlet of a low-pressure turbine cascade, operating at $\mathrm{M_{in}} \sim 0.4$ – 0.5. Due to the low-density environment, the wires were operating in the slip flow regime, with a Knudsen number around ∼0.1. The maximum fluctuations of total temperature T_0' expected in the facility were in the order of 0.05–0.1 K. It was estimated that the contribution of T_0' in Eq. (7) was at least one order of magnitude smaller compared to the contribution brought by ρ' and u' terms. Moreover, the pitch angle fluctuations were expected to be smaller than 0.5 deg, and for such range, according to Bruun [1], $S_\beta \sim 0$. For these reasons, the total temperature and pitch angle fluctuating terms were neglected, and the following sensitivity equation was employed:

$$\frac{E_b'}{\overline{E_b}} - S_\alpha \cdot \alpha' = S_\rho \cdot \frac{\rho'}{\overline{\rho}} + S_u \cdot \frac{u'}{\overline{u}} \tag{18}$$

3 Measurements Setup and Apparatus

The CTA measurements presented in this work were performed at the inlet of a low-pressure turbine linear cascade, in the high-speed low-Reynolds facility S-1/C of the von Karman Institute for fluid dynamics.

3.1 Turbine Rig. The S-1/C rig (Fig. 1) is a closed-loop wind tunnel driven by a 615 kW axial compressor, which controls the amount of mass flow by adjusting its rotational speed, while the pressure is regulated by a vacuum pump, allowing to reach minimum absolute pressures of the order of 5000 Pa. Past the compressor, the flow goes across a cooler, employed to lower the temperature to near-ambient one. Subsequently, the flow passes through a divergent section, functioning as settling chamber and equipped with wire meshes and honeycombs. A rectangular duct finally delivers the flow to the test section. A more detailed description of the facility can be found in Ref. [16]. In the present analysis, the test section was equipped with a linear cascade of 23 airfoils, with a span of 165 mm and a pitch of 32.95 mm. The measuring plane of the present investigation is indicated as "Plane 02" in Fig. 2(*a*). This plane, located 0.5 axial chords (C_{ax}) upstream of the blade leading edge plane, featured an inclination of 40.73 deg with respect to the rectangular duct cross section. In order to obtain the desired level of turbulence, the test section was equipped with a passive turbulence grid (TG), presented in Fig. 2(*b*), placed perpendicularly to the test section inlet, at a distance of 400 mm to the central blade leading edge. It consisted of 41 cylindrical rods of 3 mm in diameter, with a spacing between their centerlines of 12 mm. According to the correlation proposed by Roach [17], the expected value of turbulence intensity Tu generated by the grid at the measuring plane was around 2.5%. A spoked-wheel type wake generator (WG), consisting of a brass disk of 625 mm in diameter and with 96 bars of 1 mm in diameter, was employed to recreate the effect of unsteady incoming wakes, as

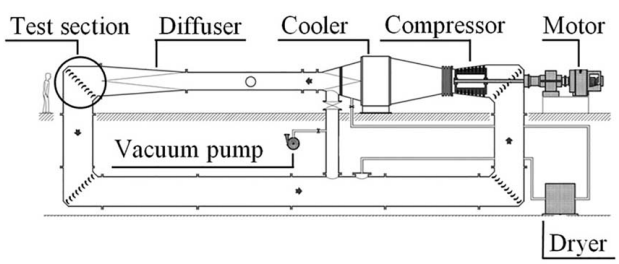

Fig. 1 Schematic of the S-1/C facility

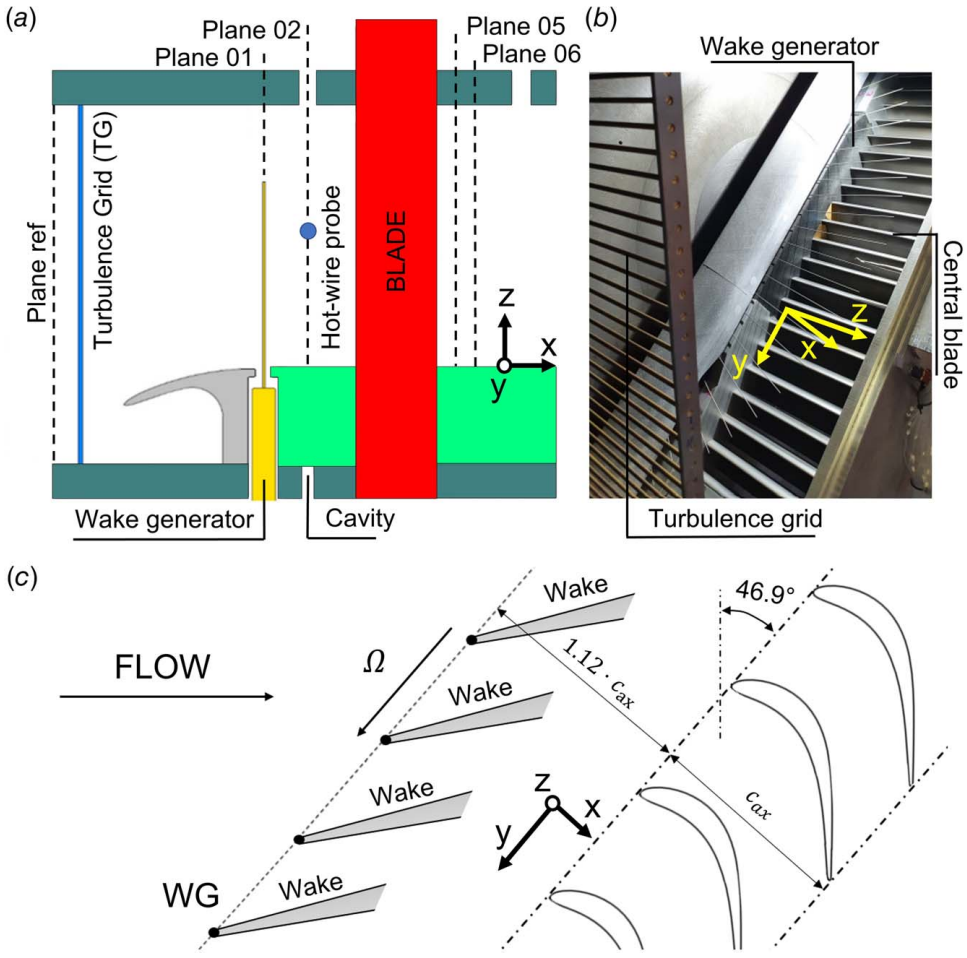

Fig. 2 (*a*) Schematic of the test section, (*b*) the TG and the WG at the cascade inlet, and (*c*) unsteady wakes at the cascade inlet

shown in Figs. 2(*b*) and 2(*c*). The wake reduced frequency was on the order of ∼0.95, resulting in a flow coefficient, computed as the ratio of the inlet axial velocity to the peripheral velocity of the bars, of 0.80. When the WG was employed, the inclination of Plane 02 with respect to the duct was changed to 46.9 deg. Geometrical details about the linear cascade and the flow conditions are reported in Table 1. Further details of the test case were provided by Simonassi et al. [18].

3.2 Instrumentation. For the present work, two different in-house built hot-wire probes were employed (Fig. 3). The first probe was a cross-wire (XW) probe, featuring two slanted wires forming an angle of 120 deg. Following the guidelines provided by Yablochkin and Cukurel in Ref. [14], the two wires were chosen with different diameters, 5 μm and 9 μm, with the purpose of obtaining different sensitivities S_u and S_ρ for the two wires. The cutoff frequency of both wires was optimally adjusted with a square-wave test at the turbine operating conditions, and was found to be around 10 and 20 kHz for the 9 μm and 5 μm wires, respectively. Due to a failure of the XW probe, the tests with the WG were performed with a single-wire (SW) probe, equipped with a single 9 μm sensor with active length of 0.7 mm and cutoff frequency around 10 kHz. A *Dantec Dynamics StreamLine Pro* anemometer was employed during the measurements. The signals were filtered with a 100 kHz analog anti-aliasing low-pass filter prior to digital sampling. A 16-bit *NI* board was used to digitize the hot-wire signal, at 300 kHz for the tests without the WG, and 1200 kHz for the experiments with the WG. A *Dantec Dynamics* calibration nozzle was used to perform the ex situ calibration.

Table 1 Details of test section geometry and flow conditions

Quantity	Value	Units
Cascade chord C	52.28	mm
Cascade axial chord C_{ax}	47.61	mm
Cascade pitch g	32.95	mm
Cascade span s	165	mm
Number of blades N_b	23	mm
Inlet Mach number M_{in}	∼ 0.46	–
Inlet Reynolds number $Re_{in,C}$	∼ 45k	–
Inlet total temperature $T_{0,in}$	∼ 300	K
Inlet total pressure $p_{0,in}$	∼9000	Pa
Inlet velocity u_{in}	∼ 160	$m \cdot s^{-1}$
Inlet density ρ_{in}	∼ 0.097	$kg \cdot m^{-3}$
Knudsen number Kn (9 μm wire)	∼ 0.1	–
Outlet Mach number M_{out}	∼ 0.90	–
Outlet Reynolds number $Re_{out,C}$	∼ 70k	–
Wake reduced frequency f^+	∼ 0.95	–

4 Calibration and Data Reduction Methodology

Being the hot wires operated in a compressible slip flow, a nondimensional calibration approach was adopted and a sensitivity-based postprocessing technique was implemented to decouple the velocity and the density fluctuations.

4.1 Cross-Wire Probe Calibration and Data Reduction. The XW calibration can be essentially divided into two different steps: a low-speed ex situ calibration, to determine the wire

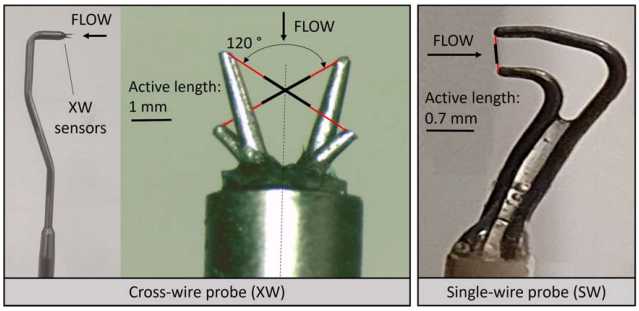

Fig. 3 Cross-wire (left) and single-wire (right) probes heads

temperatures T_w and the angular response, and an in situ calibration to obtain the Nu − Re_w − Kn correlations and compute the wire sensitivities.

4.1.1 Determination of Wire Temperature. The effective wire temperature T_w is the temperature that best represents the convective heat transfer between the hot wire and the flow. This value typically differs from the temperature imposed by the user during the hot-wire setup, since the temperature distribution is not uniform over the whole wire length. The temperature T_w is defined as the one collapsing a set of Nu-Re_w data, obtained at different flow temperatures, on a single fourth-order polynomial curve. To determine its value, a low-speed calibration was carried out in the *Dantec* calibration nozzle (*StreamLine*® *Pro Automatic Calibrator*), where flow velocity and total temperature were varied systematically in the range ∼0 – 50 m/s and ∼20 – 40 °C, as shown in Fig. 4(*a*). During the calibration, the probe head was kept in a fixed (reference) position, aligned with the incoming flow, as shown in Fig. 3. For low-speed continuum flows, the Nusselt number is a unique function of the Reynolds number and was computed with Eq. (5), while the Reynolds number was calculated with Eq. (2). The Nusselt number was computed for a set of expected T_w, and the value providing the best R^2 of the polynomial interpolation was selected [6]. The results are reported in Fig. 4(*b*), and the wire temperatures were found to be $T_{w_1} = 400.4$ K and $T_{w_2} = 456.8$ K.

4.1.2 Angular Calibration. The angular calibration was carried out in the same low-speed jet facility, following the methodology proposed by Cukurel et al. [6]. The probe was yawed in an angular range of −40 deg to +40 deg, for different conditions of u and T_0. The Nu − Re_w curves computed to determine T_w (Fig. 4(*b*)) were exploited to compute $\mathrm{Re}_{\mathrm{eff}_1}$ and $\mathrm{Re}_{\mathrm{eff}_2}$, where the subscript "eff" indicates the effective Reynolds number, i.e., the one that would yield to the same Nusselt number if the probe were aligned at the reference position. These values were then normalized by the $\mathrm{Re}_{\alpha_{0,1}}$ and $\mathrm{Re}_{\alpha_{0,2}}$, where the subscript "$\alpha_0$" denotes the values that would be computed at the reference position. The formulation is given as follows:

$$\frac{\mathrm{Re}_{\mathrm{eff}_1}}{\mathrm{Re}_{\alpha_{0,1}}} = f_1(\alpha); \quad \frac{\mathrm{Re}_{\mathrm{eff}_2}}{\mathrm{Re}_{\alpha_{0,2}}} = f_2(\alpha) \tag{19}$$

The resulting curves are reported in Fig. 5(*a*). As expected, the two curves $f_1(\alpha)$ and $f_2(\alpha)$ show an opposite and symmetric trend. When a XW probe is yawed in the jet, one of the two wires gets more orthogonal to the flow, experiencing a higher normal velocity, i.e., a higher cooling, while the opposite occurs on the other wire. A higher cooling corresponds to a higher bridge voltage E_b, which translates in a higher Nu and consequently in a higher $\mathrm{Re}_{\mathrm{eff}}$. In the scope of the present work, and in agreement with the conclusions in Refs. [6,15], no variations in the angular response, expressed in the form of Eq. (19), were detected for different Reynolds and Mach numbers and flow total temperature values. Consequently, a single curve regression, performed on the low-speed ex situ data, was assumed to be representative of the angular response independently of the actual flow velocity, density, and total temperature. The yaw angle was then expressed as a unique function of the two effective Reynolds numbers, yielding to:

$$\alpha = F\left(\frac{\mathrm{Re}_{\mathrm{eff}_2}}{\mathrm{Re}_{\mathrm{eff}_1}}\right) \tag{20}$$

The results are shown in Fig. 5(*b*). From the same dataset, the yaw angle sensitivity correlation was built in the form $S_\alpha = f(\alpha, \mathrm{Nu})$.

4.1.3 In Situ Calibration. Since the vacuum and transonic flow conditions encountered during the actual tests (Table 1) could not be replicated in an open jet facility, the nondimensional mass flux calibration was performed *in situ*. A total of 14 calibration points were collected for different levels of Re_w and M. During the in situ operations, due to the combination of high flow velocities and low densities, the flow around the wires was in the slip regime, with a Knudsen number on the order of 0.1. In compressible and rarefied flows, Eq. (5) applies: the dependency of Nu on both Re_w and M is highlighted in Fig. 6(*a*), where scattered and discontinuous points are visible around M = 0.4 for the 9 μm wire dataset. The same trend was also detected for the 5 μm wire. In order to apply the angular calibration (Eq. (20)), the Reynolds number time series of both wires were required, but scattered calibration points could not be used for this purpose. To obtain continuous

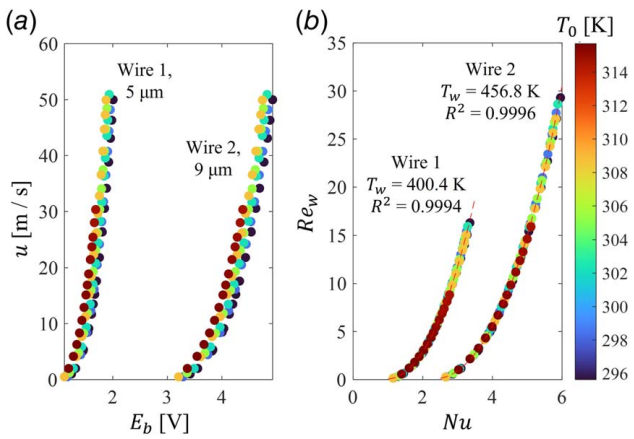

Fig. 4 Low-speed calibration to determine T_w: (*a*) dimensional curves and (*b*) nondimensional curves

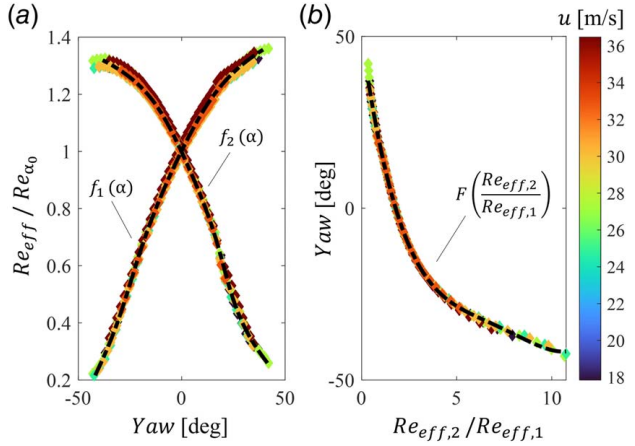

Fig. 5 Cross-wire probe angular calibration: (*a*) response of the two sensors and (*b*) unique angular calibration curve

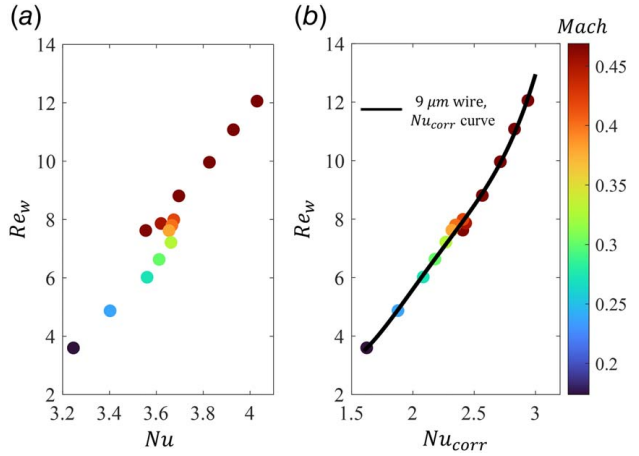

Fig. 6 (*a*) In situ calibration data and (*b*) corrected calibration curve for the 9 μm wire

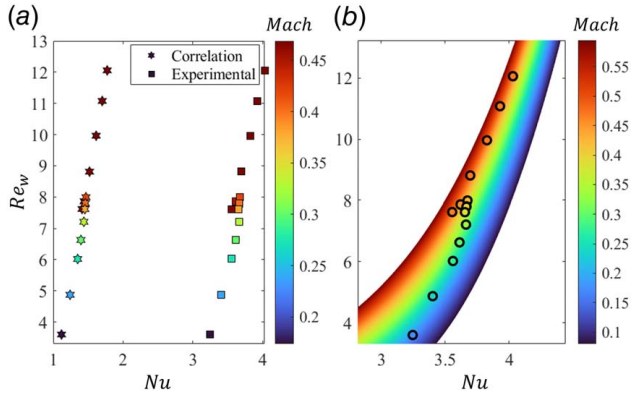

Fig. 7 (*a*) Experimental data compared to the correlation of Xie et al. [19] and (*b*) nondimensional calibration map

curves, the Nusselt number was corrected exploiting the correlations of Dewey [8] (Eq. (6)) and Klopfer [10]. The resulting $\mathrm{Nu_{corr}}$ curves were assumed to be Mach independent, so Re_w was uniquely a function of $\mathrm{Nu_{corr}}$, as shown in Fig. 6(*b*).

If a $\mathrm{Nu_{corr}} - Re_w$ calibration curve is adopted, the link between the physical Nusselt number (Nu) and the corrected one $\mathrm{Nu_{corr}}$ is the Dewey's correcting factor $\phi = f(\mathrm{Re}_w, \mathrm{M})$. Therefore, the hot-wire sensitivities to density and velocity could be computed through the differentiation of ϕ with respect to Re_w and M, exploiting Eqs. (14) and (15). In the present case, this approach led to nonphysical negative values of velocity sensitivity S_u for both wires. This observation suggested that Dewey's correlation, whose range of validity was defined by a range of M, but not of Kn, is inaccurate when used to compute the hot-wire sensitivities in slip flow regimes, for $\mathrm{Kn} \sim 0.1$. For this reason, the $\mathrm{Nu_{corr}} - \mathrm{Re}_w$ curves were employed uniquely to obtain Re_w time series, used then to compute the fluctuating yaw angle by means of Eq. (20), but not to calculate S_ρ and S_u. To accurately determine the density and velocity sensitivities directly applying Eqs. (11) and (12), $\mathrm{Nu} - \mathrm{Re}_w - \mathrm{Kn}$ or $\mathrm{Nu} - \mathrm{Re}_w - \mathrm{M}$ functions were thus necessary. A recent numerical work of Xie et al. [19] proposed a correlation to describe the heat transfer for infinite cylinders, valid in the slip flow regime ($0.01 < \mathrm{Kn} < 0.1$) and for $0.1 < \mathrm{Re}_w < 20$:

$$\mathrm{Nu} = 0.2491 + 0.5589\mathrm{Re}_w{}^{0.4573} - 0.6245\mathrm{Re}_w{}^{0.5639}\mathrm{Kn}^{0.8565} \quad (21)$$

In Eq. (21), the Mach number does not appear explicitly, but was incorporated into the Knudsen number. Although it might seem a minor difference, this formulation suggested that the heat transfer in slip flows is not driven by the Mach number, i.e., by the effect of flow compressibility, but is actually governed by the degree of rarefaction of the gas, i.e., the Knudsen number. The same conclusion was drawn by Nagabushana and Stainback [9]. Equation (21) was applied to determine the Nusselt number, and very similar trends with respect to the experimental calibration points were found. However, the Nusselt number estimated by Eq. (21) was always smaller than the experimental values. As an example, the difference between the Nusselt number computed with the correlation of Xie et al. [19] and the experimental data for the 9 μm wire is presented in Fig. 7(*a*). This offset was thought to be related to the heat conduction between the hot-wire sensor and the prongs, neglected in the Nusselt number formulation of Eq. (3) and leading to a Nusselt number overestimation. Although almost constant, this offset could not be ignored in the presence of a logarithmic differentiation, thus S_ρ and S_u could not be obtained directly differentiating the correlation. So, in order to apply Eqs. (11) and (12), a $\mathrm{Nu} - \mathrm{Re}_w - \mathrm{Kn}$ interpolation on the calibration points was mandatory. Following the methodology of Xie et al. [19], a Levenberg–Marquardt nonlinear fitting was performed on the experimental dataset. Due to the small number of experimental points, a simpler function, with the following form, was adopted:

$$\mathrm{Nu} = A + B\mathrm{Re}_w{}^{C} + D\mathrm{Kn}^{E} \quad (22)$$

The calibration coefficients are presented in Table 2.

The resulting calibration map for the 9 μm sensor is shown in Fig. 7(*b*) as a function of Re_w and M. The figure clearly shows that the dependency of the Nusselt number on the Mach number goes well below the "compressibility limit" of $\mathrm{M} = 0.3$, which is also the lower bound of the correlation of Dewey. This observation suggested that the $\mathrm{Nu} - \mathrm{Re}_w - \mathrm{Kn}$ function of Eq. (22) is necessary to accurately describe the heat transfer physics in the slip flow regimes.

4.1.4 XW Postprocessing Methodology. The proposed postprocessing methodology for the XW probe follows:

- The unsteady voltages of the two wires were digitally filtered at 30 kHz and resampled at 70 kHz.
- The local flow total temperature $\overline{T_0}$ was known from thermocouple measurements. Similarly, the local time-averaged Mach ($\overline{\mathrm{M}}$), Reynolds ($\overline{\mathrm{Re}_{w_{1,2}}}$), and Knudsen ($\overline{\mathrm{Kn}_{1,2}}$) numbers were retrieved from five-hole pressure probes measurements and from the knowledge of the inlet total pressure $p_{0,\mathrm{in}}$.
- Equation (3) was applied to compute time series of the two wires Nusselt number ($\mathrm{Nu}_{1,2}$). The time series of $\mathrm{Nu}_{1,2}$ were then converted into $\mathrm{Nu}_{\mathrm{corr}_{1,2}} = f(\overline{\mathrm{Re}_{w_{1,2}}}, \overline{\mathrm{M}}, \mathrm{Nu}_{1,2})$, exploiting Dewey's correlation.
- The time series of $\mathrm{Nu}_{\mathrm{corr}_{1,2}}$ were converted in time series of $\mathrm{Re}_{w_{1,2}}$ through the $\mathrm{Nu_{corr}} - \mathrm{Re}_w$ calibration curves.
- Using the angular calibration curve of Eq. (20), the ratio of Re_{w_1} and Re_{w_2} provided the angular fluctuations α'.
- The sensitivities S_ρ and S_u were computed with Eqs. (11) and (12), from the calibration map of Eq. (22), while the angular sensitivity S_α was computed exploiting Eq. (16).

The adoption of the XW probe, featuring two wires, allows the decoupling of two turbulent quantities in the sensitivity equation. As previously discussed, in the present work, the total temperature and pitch angle fluctuating terms were neglected. Thus, Eq. (18) was used to build a 2-by-2 sensitivity system, in order to decouple

Table 2 Calibration coefficients for the XW probe

Wire	d_w (μm)	A	B	C	D	E
W1	5	1.045	0.601	0.314	−2.177	0.900
W2	9	2.584	0.708	0.386	−3.588	0.768

ρ' and u':

$$\begin{bmatrix} S_{\rho_1} & S_{u_1} \\ S_{\rho_2} & S_{u_2} \end{bmatrix} \begin{bmatrix} \frac{\rho'}{\overline{\rho}} \\ \frac{u'}{\overline{u}} \end{bmatrix} = \begin{bmatrix} \frac{E_1'}{\overline{E_1}} - S_{\alpha_1}\alpha' \\ \frac{E_2'}{\overline{E_2}} - S_{\alpha_2}\alpha' \end{bmatrix} \tag{23}$$

The solution of the sensitivity system provided a time series of ρ' and u'. The turbulence intensity Tu was then computed as follows:

$$\mathrm{Tu} = \frac{\sqrt{u'^2}}{\overline{u}} \tag{24}$$

For the integral length scale computation, the formulation proposed by Roach [17] was exploited assuming isotropic turbulence:

$$\Lambda_x = \left[\frac{E(f)\overline{u}}{4u'^2}\right]_{f\to 0} \tag{25}$$

where $E(f)$ is the power spectrum of the velocity fluctuations, extrapolated for a frequency value approaching zero. To compute this value, the power spectrum was averaged up to a frequency before the decay, as discussed later in Sec. 5.

4.2 Single-Wire Probe Calibration and Data Reduction. The calibration procedure for the single-wire probe is very similar to that of the XW probe. The wire temperature was determined by means of the same low-speed calibration, but no angular calibration was required, since a single-wire probe is not suitable to measure instantaneous flow angles. The in situ calibration was obtained through the same $\mathrm{Nu} - \mathrm{Re}_w - \mathrm{Kn}$ mapping of Eq. (22), allowing to compute the wire sensitivities. The computed calibration coefficients are reported in Table 3.

The single-wire probe did not allow to decouple density from velocity. So, the density fluctuations had to be assumed negligible and Eq. (18) was simplified to:

$$\frac{u'}{\overline{u}} = \frac{1}{S_u}\frac{E_b'}{\overline{E_b}} \tag{26}$$

providing as output a time series of unsteady velocity fluctuations. The turbulence intensity and the integral length scales were then computed using Eqs. (24) and (25). The measurements of the time-resolved turbulence field downstream the rotating WG were performed by means of the SW probe. In order to provide a comparison between the two data reduction methodologies (Eqs. (23) and (26)), and to quantify the impact of the assumption of negligible density fluctuations, the voltage time series of the 9 μm wire of the XW probe were also postprocessed by means of Eq. (26).

5 Results and Discussion

In this section, the results of the steady and unsteady measurements, i.e., without and with WG, are discussed. All the tests were conducted at the cascade inlet at blade midspan, traversing the hot-wire probes over two blade pitches, from $y = -g$ to $y = g$. The position $y = 0$ indicates the pitchwise coordinate of the leading edge of the cascade's central blade.

5.1 Hot-Wire Sensitivities. Before discussing the resulting turbulence parameters, the computed hot-wire sensitivities are presented and compared with the available literature. The sensitivities to density and velocity for the two probes are plotted in Fig. 8. It is

Table 3 Calibration coefficients for the single-wire probe

T_w (K)	A	B	C	D	E
616	3.119	0.696	0.301	−5.276	0.613

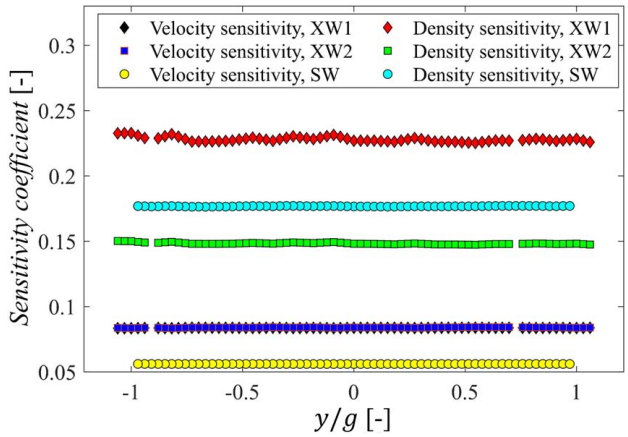

Fig. 8 Sensitivities to density and velocity for the two hot-wire probes

immediately apparent that the density sensitivities were systematically higher than those to velocity, and this result is in agreement with all values reported in literature for compressible flows [3,6,9,13]. In the present case, only the 5 μm wire (XW1) presented a S_ρ higher than 0.2, while the two 9 μm wires (XW2 and SW) are on the order of 0.15 and 0.175, respectively. The velocity sensitivities were found to be around 0.08 for both XW1 and XW2 and on the order of 0.055 for the SW. These trends are different from the ones reported by Cukurel et al. [6], where a 9 μm wire presented higher sensitivities to density and velocity compared to a 5 μm wire. To justify these differences, it is worth mentioning that the present investigation was performed in a compressible and rarefied flow, with $\mathrm{Kn} \sim 0.1$, while the work in Ref. [6] was performed at atmospheric pressure conditions. Moreover, in the work in Ref. [6], the sensitivities were computed starting from a $\mathrm{Nu}_{\mathrm{corr}} - \mathrm{Re}_w$ curve, thus performing a direct derivative of Dewey's correlation using Eqs. (14) and (15). As previously discussed, this approach led to nonphysical values of velocity sensitivity when applied to the present dataset.

5.2 Steady Measurements

5.2.1 Power Spectra. For turbulent signals, the power spectral density (PSD) represents the turbulent spectra of the energy cascade, and its integral provides the standard deviation of the velocity fluctuations, i.e., the turbulence intensity. The spectral analysis thus allows the identification of sources of turbulence and provides information about how the energy of the signal is distributed with respect to the frequency. Two spectra obtained through the classical *pwelch* function, for the cases with and without the TG, are presented in Fig. 9. It is possible to identify the turbulent inertial subrange, characterized by the −5/3 slope, starting around 3 kHz for the freestream flow and around 5 kHz for the flow perturbed by the TG. However, these spectra were noisy and spurious peaks appeared in the PSD at frequencies of 6 kHz, 10.4 kHz, 12.5 kHz, 16.3 kHz, 20.5 kHz, and 23.7 kHz. Their presence was not related to any flow fluctuations, since the wake generator was not employed for steady measurements, and could not be ascribed to vortex shedding from the TG bars since they were present even in the absence of the TG. Consequently, the spurious peaks could only be related to the facility itself, perhaps due to vibrations generated by the compressor or the vacuum pump, or to resonances of the hot-wire probe. Moreover, a noisy spectrum makes it difficult to extrapolate at zero frequency to compute the integral length scales (Eq. (25)), so the peaks had to be eliminated to perform proper measurements. Median and Savitzky–Golay filters were hence applied to smooth the spectra, as suggested by Heckmeier et al. [20]. A filtered spectrum is presented in Fig. 10 by the red line: the fluctuations were significantly

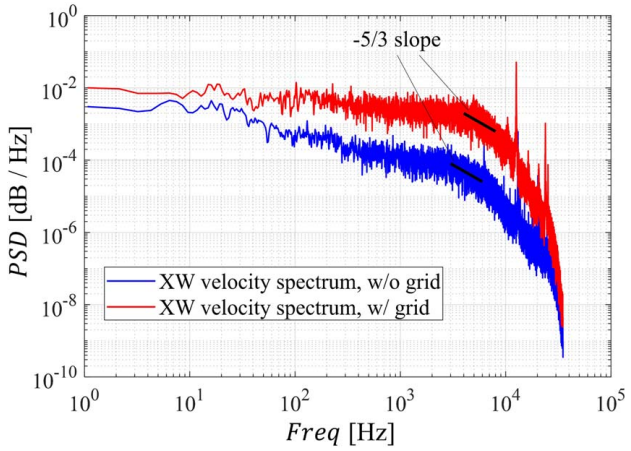

Fig. 9 Velocity spectra comparison, with and without the turbulence grid, for the XW probe

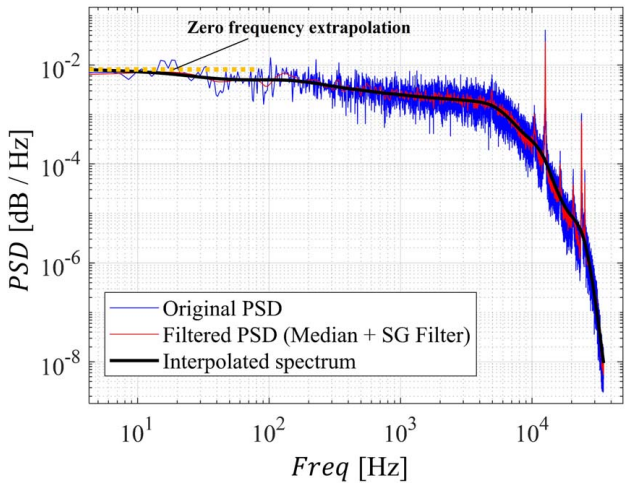

Fig. 10 Steps for smoothing the spectra

reduced, allowing a safer zero-frequency extrapolation, but the spurious peaks were still persistent. For this reason, a tailor-made smoothing spline fitting (black line in Fig. 10) was performed in few tests, in order to cancel out the peaks and determine their impact on the turbulence intensity computation. The standard deviation of the velocity fluctuations was then computed as follows:

$$\sqrt{u'^2} = \sqrt{\int \mathrm{PSD}(f)\,\mathrm{d}f} \tag{27}$$

After applying Eq. (27) to the smoothed spectrum, the turbulence intensity was recomputed. The boost in turbulence intensity due to the spurious peaks was finally found to be negligible for the tests without the TG (approximately 0.03%) and around 0.25% for the tests with the TG.

5.2.2 Turbulence Intensity. The turbulence intensity values, computed with Eq. (24), are shown in Fig. 11. The caption "XW" refers to the results obtained from the sensitivity system postprocessing methodology (Eq. (23)). As previously explained, Eq. (26) was also used, treating the 9 μm wire of the XW probe as a single wire, in order to understand the influence of neglecting the ρ' contribution. These results are indicated by the caption "1W." According to a previous investigation performed in the same rig, Tu naturally achieved by the facility was expected to be around 0.9% [21]. In the present investigation, the results were slightly lower, and the

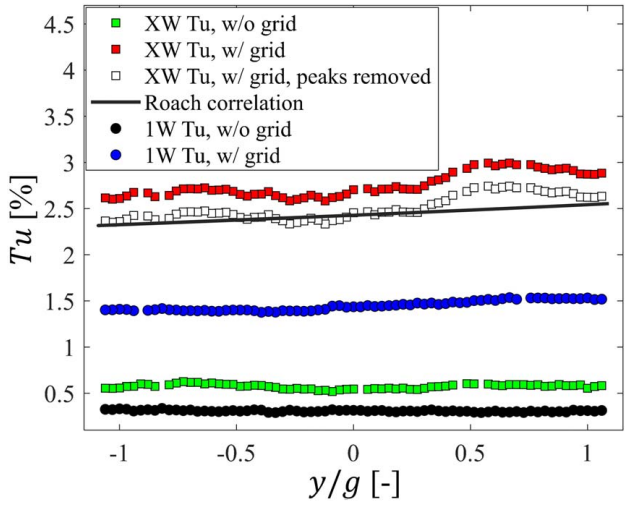

Fig. 11 Turbulence intensity, with and without the turbulence grid

Tu measured by the XW without the grid was around 0.55%. The results obtained with the single-wire method were even lower (Tu ~ 0.3%). A bigger difference between the two processing methodologies was observed for the tests with the TG. The XW method provided a Tu bounded between 2.5% and 3%. As previously discussed, the estimated boost of Tu imputable to the spurious peaks in the spectra was around 0.25%. The corrected Tu values, obtained by removing this offset, are also presented in Fig. 11. These results are in fair agreement with Tu predicted for grid-generated turbulence by Roach's model [17], shown by the black continuous line in Fig. 11. The single-wire method provided a significantly lower value of Tu, between 1.4% and 1.5%, proving that neglecting the density fluctuations in such a high-speed low-density flow is a questionable assumption, leading in this case to a severe underestimation of Tu by ~1%. This evidence suggested that a sensitivity-based system (Eq. (23)) is mandatory to decouple density and velocity fluctuations in compressible slip flows applications.

5.2.3 Integral Length Scales. The traditional approach to compute integral length scales is based on the autocorrelation function of the velocity signal [17]. However, when this approach is employed on experimental datasets, the noise can offset the integral length scale value, resulting in extremely variable test-to-test results. As an example, for the tests without the TG, this method provided integral length scales oscillating in the order of $300 < \Lambda_{\mathrm{int}} < 700$ mm. The same trend was highlighted by Michálek et al. [21], who showed that low-frequency large-scale patterns, of the same dimension of the connecting duct (~0.5 m) developed in the test section if the TG was not employed. In order to eliminate the low-frequency scales and to reduce the test-to-test variability, a different approach, based on Eq. (25), was employed in the scope of this study. To apply Eq. (25), a zero-frequency extrapolation in the PSD was performed, averaging the spectra over a certain range of low-frequencies, as shown in Fig. 10. Looking at the spectra of Fig. 9, a high-energy content at low frequencies is discernible for the tests without the TG, in agreement with the conclusions of Michálek et al. [21]. The spectrum drops and stabilizes in a region around 100 Hz. For this reason, the zero-frequency extrapolation, for the tests without the TG, was performed averaging the spectra between 100 Hz and 400 Hz, canceling out the low-frequency content associated with the largest low-frequency scales. On the other hand, the spectrum for the test with the TG flattened out at low frequencies, indicating that the large-scale structures previously detected were no longer dominant. Accordingly, for the tests

with the TG, the zero-frequency extrapolation was performed averaging the PSD between 0 Hz and 100 Hz. The results are presented in Fig. 12, where the integral length scales are shown to be between 14 mm and 19 mm for the tests without the TG, and between 10 mm and 15 mm for the tests with the TG. In particular, the results with the TG suggested that the dominant structures were associated to scales of the same order of the mesh size of the TG. The computed values were comparable to the ones reported by Michálek et al. [21], amounting to 30 mm and 12 mm for the tests, respectively, without and with the TG. For the sake of completeness, the results obtained averaging the PSD of the tests without the TG between 0 Hz and 100 Hz, as well as the ones with the TG if the averaging was performed from 100 Hz to 400 Hz, are shown in Fig. 12. As expected, without the grid, the integral length scales resulting from an averaging at low frequencies were significantly higher, between 50 mm and 80 mm. On the other hand, if the tests with the TG were averaged between 100 Hz and 400 Hz, no major differences could be identified, just a small reduction of ~3 mm. This trend was again justified by the fact that, in the presence of the TG, the spectra appeared almost flat in the whole range from 0 to 400 Hz, as shown in Figs. 9 and 10.

The integral length scales were found to be of the same order of magnitude when using the processing methodology of the single wire. However, these results showed an opposite trend, with higher scales ($\Lambda_{int} \sim 18$ mm) for the tests performed with the TG, and lower values ($\Lambda_{int} \sim 14$ mm) for the tests in the absence of the TG. This trend, opposite to the experimental evidence previously discussed, and to the findings reported in Ref. [21], suggested that an accurate estimation of the velocity fluctuations u', decoupled from the density fluctuations ρ' through Eq. (23), is mandatory to correctly estimate Λ_{int} with Eq. (25).

The time-average pitchwise average measurements of turbulence intensity and integral length scales are summarized in Table 4.

5.2.4 Angle and Density Fluctuations. The proposed experimental methodology provided also the unsteady fluctuations of yaw angle and density. The intensity of the density fluctuations was determined to be around 0.25% and 1.1% for the tests performed without and with the TG, respectively. On the other hand, the standard deviation of the yaw angle fluctuations was found to be around 0.35 deg when the tests were performed in the presence of the TG, with the fluctuations bounded in the interval ± 1.5 deg. For the tests performed without the TG, the standard deviation of α' reduced to approximately 0.1 deg, and all the fluctuations were bounded in the interval ± 0.5 deg.

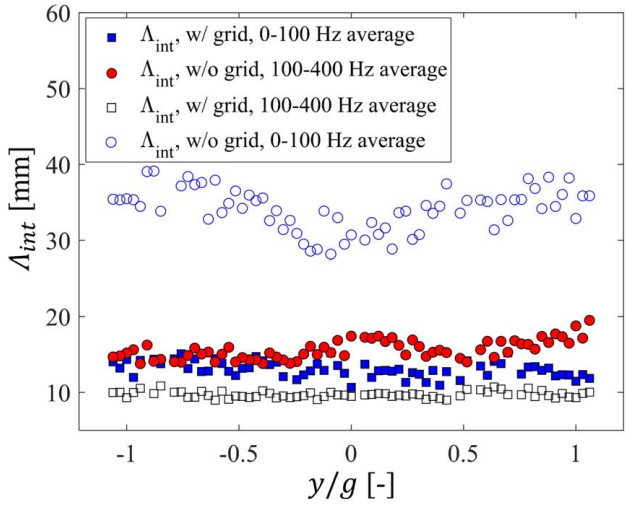

Fig. 12 Integral length scales, with and without the turbulence grid

Table 4 Tu and Λ_{int}, steady measurements

Quantity	Value	Units
Without the TG		
Tu, XW	0.55	%
Tu, 1W	0.30	%
Λ_{int}, 0–100 Hz avg.	60	mm
Λ_{int}, 100–400 Hz avg.	17	mm
Λ_{int}, Michálek et al. [21]	30	mm
With the TG		
Tu, XW	2.7	%
Corrected Tu, XW	2.5	%
Tu, 1W	1.5	%
Λ_{int}, 0–100 Hz avg.	12	mm
Λ_{int}, 100–400 Hz avg.	10	mm
Λ_{int}, Michálek et al. [21]	12	mm

5.2.5 Uncertainty Analysis. Due to the complexity of the XW postprocessing methodology, the uncertainty analysis was carried out implementing a Monte Carlo algorithm across the whole measurement chain, from the in situ calibration to the postprocessing of the experiments, following the methodology proposed by Boufidi et al. [7]. Two major sources of uncertainity were identified in this analysis, namely, the uncertainty of the accessory measurements and the fitting error in the calibration laws. For each of the N_i Monte Carlo iterations, the uncertainties of the accessory measurements of total pressure, static pressure and total temperature, used to define the operating point of the facility were divided in random and bias errors and randomly perturbed around their statistical distribution. In order to compute Nusselt, Mach, Reynolds, and Knudsen numbers, accessory thermocouple and five-hole pressure probe measurements were required, and this uncertainty contribution was accounted too. For all the input values, rectangular and Gaussian distributions were used to account for the bias and random errors, respectively. The complete breakdown in random and bias errors of all the input quantities can be found in the SPLEEN open-source database [22].

A set of N_i $Nu_{corr} - Re_w$ and $Nu - Re_w - Kn$ calibration laws was generated and used to solve the sensitivity system. Due to the scarcity of the calibration points, the error imputable to the two fittings was propagated in the sensitivity system estimating the 95% confidence interval of the calibration laws around each measuring point (in terms of average Mach, Reynolds, and Knudsen numbers) and treating it as a random contribution, as suggested by Boufidi et al. [7]. The convergence on the turbulence statistics was reached approximately after $N_i = 5000$ iterations. The resulting distributions of turbulence intensity were found to be mildly positively skewed, following a log-log-normal distribution. The 95% confidence intervals around the Tu mean value were found to be [−0.35% ; +0.48%] for the tests with the TG, and [−0.09% ; +0.14%] in the absence of the TG. Similarly, the non-symmetric 95% confidence intervals for the integral length scales were determined to be [−0.6 mm; +2.3 mm] and [−1.3 mm; +0.3 mm] for the tests with and without the TG, respectively.

5.3 Unsteady Measurements. The results presented in this section refer to the unsteady tests, carried out with the WG, a set of 96 rotating bars shedding wakes at engine-representative reduced frequencies ($f^+ = 0.95$), corresponding to a bar-passing frequency around 5.3 kHz. All tests were performed with the SW probe; thus, Eq. (26) was exploited to retrieve the turbulent velocity fluctuations. As highlighted in the previous section, neglecting the density fluctuations is an oversimplification that led to an underestimation of the Tu of ~1% for the tests performed with the TG. As a consequence, the unsteady measurements presented in this section are expected to be less accurate, compared to the steady ones, and can provide qualitative trends, but not high-fidelity quantitative results.

In the presence of periodic phenomena, turbulence measurements are challenging, since it is necessary to distinguish the deterministic unsteadiness from the stochastic fluctuations required to compute turbulence parameters. The PSD of the velocity fluctuations obtained through Eq. (26) is shown in black in Fig. 13. This spectrum presents two distinct peaks at 5.3 kHz and 10.6 kHz, corresponding to the bar-passing frequency and its first harmonic. Other smaller peaks, between 3 kHz and 9 kHz, are also distinguishable. To remove these deterministic components, the velocity signals were ensemble averaged using the phase-locked averaging (PLA) technique. For a periodic quantity, the method consists in averaging the signals over several repeating periods, N_{per}. The period of each event was discretized in several classes, N_{class}, and the points belonging to the same class were averaged to obtain the final ensemble-averaged signal. The PLA method, for a velocity signal $u(t)$, can be defined mathematically in Eq. (28):

$$u_{PLA}(t_i) = \frac{1}{N_{per}} \sum_{j=1}^{N_{per}} u_j(t_i), \quad i = 1 \ldots N_{class} \tag{28}$$

The fluctuating component u_{PLA} was then removed from the original velocity time series, eliminating the deterministic contributions while preserving the turbulent fluctuations $u_{turb}(t)$:

$$u_{turb}(t) = u(t) - u_{PLA} + \overline{u_{PLA}} \tag{29}$$

The time-average turbulence intensity was then computed applying Eq. (24) to the velocity time series $u_{turb}(t)$.

In this work, the velocity time series were ensemble-averaged using two different approaches, considering as repeating periods both the full rotor revolution (disk passing frequency method (DPF)) and the single bar passage (bar passing frequency method (BPF)). Each signal was acquired for 3 s, corresponding to approximately 165 complete rotor revolutions and 15800 bar passages. The PSD of the velocity time series $u_{turb}(t)$ are shown for the two methods in Fig. 13. The peaks associated to the periodic blade passages were completely eliminated by both approaches. However, when the BPF method was employed, the PLA failed to identify the smaller peaks, suggesting that these frequency components were associated either to unsteady vibrations of the WG disk or to small differences in the wakes generated by the different bars.

In the present analysis, effort was put toward determining the phase-resolved turbulence intensity $\widetilde{Tu}$. When the ensemble-averaging was performed, the standard deviation of the velocity signal was computed for each PLA class, i.e., for every phase of the repeating event (the disk revolution for the DPF method and the bar passage for the BPF method). The phase-resolved $\widetilde{Tu}$ was then obtained applying Eq. (24) to the phase-resolved standard deviation vector. An example of phase-resolved turbulence intensity $\widetilde{Tu}$ is shown in Fig. 14. In Fig. 14(*a*), the ensemble-average was performed using the DPF method, so the 96 peaks and valleys representative of the 96 bar passages can be distinguished. The peak-to-peak and valley-to-valley variability of $\widetilde{Tu}$ highlighted how the 165 rotor revolution events of the DPF method were not enough to achieve a statistical convergence on the velocity standard deviation. This was confirmed by the results obtained with the BPF method, as shown in Fig. 14(*b*). The statistical convergence was indeed achieved after 85 rotor revolutions, corresponding to 8200 bar passage events. This result suggested that approximately 8200 full rotor revolutions would be necessary to accurately phase-resolve the turbulence intensity exploiting the DPF method. For completeness, the $\widetilde{Tu}$ obtained ensemble-averaging the DPF phase-resolved $\widetilde{Tu}$ over the 96 blade passages is reported in Fig. 14, and no significant differences were detected in the maximum and minimum values when compared to the BPF method. The peaks and valleys in Fig. 14 are associated to regions of wake-perturbed and clean flow, respectively. If the phase-locking was performed over the full rotor disk, the maximum level of $\widetilde{Tu}$ associated to the wake was approximately in the order of 6.5%, while the lower values in the clean flow region were found to be around 2%. On the other hand, using the

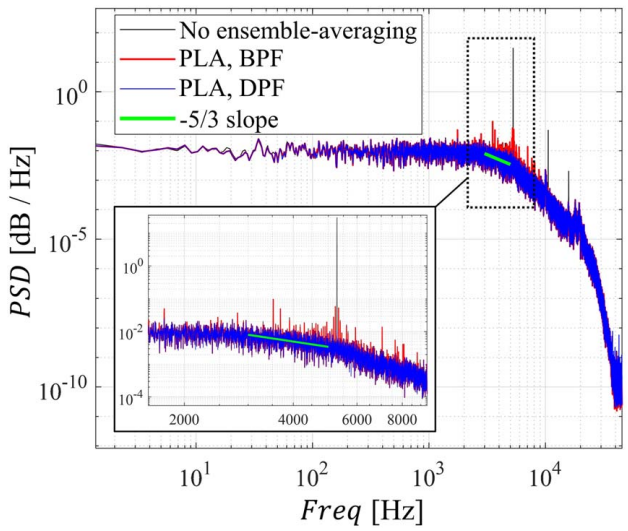

Fig. 13 Spectrum before and after applying the ensemble-averaging

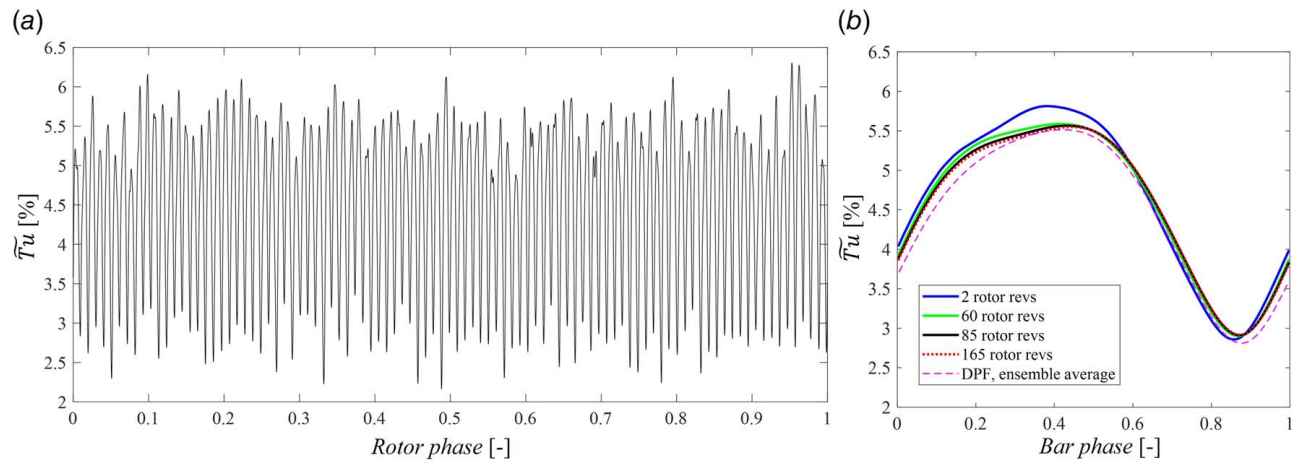

Fig. 14 Phase-resolved turbulence intensity $\widetilde{Tu}$: (*a*) DPF method and (*b*) BPF method

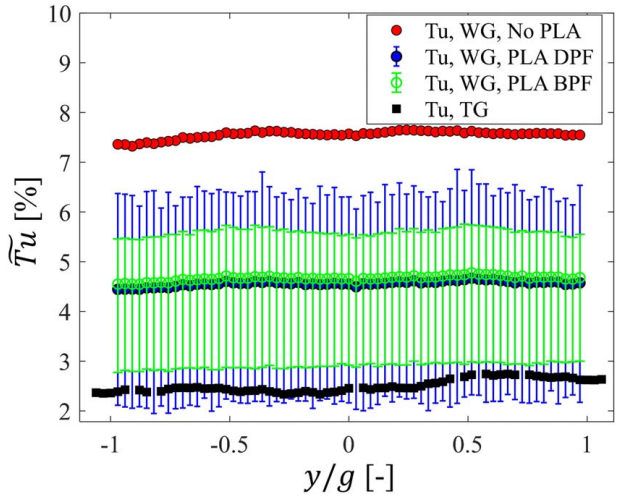

Fig. 15 Turbulence intensity, tests with the WG

BPF method, the maximum and minimum levels of $\widetilde{\text{Tu}}$ were 5.5% and 3%, respectively. In Fig. 15, the results of the time-averaged $\widetilde{\text{Tu}}$ for the full experimental dataset are shown by the blue points for the DPF method and by the green points for the BPF method. The time-average turbulence intensity was found to be in the order of 4.5% for all the experiments and for the two averaging approaches. The slightly higher values obtained using the BPF method were due to the deterministic fluctuations associated to the disk, which were not eliminated by this approach as previously shown in Fig. 13. The bar plot represents the minimum and maximum values of the phase-resolved $\widetilde{\text{Tu}}$, showing the range of the turbulence intensity oscillations for each test. For the DPF method, the peak-to-valley variation of $\widetilde{\text{Tu}}$ amounted approximately to 4.5%, again with maximum values of $\sim$6.5% and minimum values around $\sim$2%. The test-to-test variability was imputed to the statistical convergence not achieved by the DPF method. If the BPF method was used, maxima and minima were found to be almost constant for all the experiments, again in the order of 5.5% and 3%, respectively. For the sake of completeness, the turbulence intensity computed without ensemble-averaging the signal is presented in Fig. 15 in red. As expected, this value was significantly higher compared to the one obtained removing the PLA of the signal. Indeed, if Eq. (29) was not applied, the deterministic fluctuations caused by the WG were treated as stochastic and thus used to compute $\widetilde{\text{Tu}}$, leading to an overestimation of the turbulence intensity in the order of 3%.

To conclude, the DPF method allowed the removal of not only the deterministic fluctuations associated to the bar-passing frequency but also the ones due to the WG disk rotation and bar-to-bar variations. It was thus considered more reliable to compute the time-average turbulence intensity. On the other hand, the BPF method provided a significantly better statistical convergence, i.e., a better phase-resolved turbulence intensity, since the number of blade passing events was 96 times higher, when compared to the 165 disk revolutions.

6 Conclusions

In this work, the application of hot-wire anemometry in compressible rarefied flows is discussed in detail. The experiments were performed in the von Karman Institute S-1/C high-speed low-Reynolds number facility, at engine-representative flow conditions of a modern low-pressure turbine, with an inlet Mach number around 0.46 and a Knudsen number, computed with respect to the diameter of the hot wire, around 0.1. In compressible and rarefied flow regimes, a hot wire is strongly sensitive to the density fluctuations occurring in the flow, while the sensitivity to velocity is typically smaller. So, the traditional calibration and data reduction approaches suffer from inaccuracies and lead to erroneous results if the density fluctuations effect is neglected. In this article, expanding the work reported in Refs. [3,6] to slip flow applications, a novel nondimensional calibration procedure, based on the dimensionless groups $\text{Nu} - \text{Re}_w - \text{Kn}$, and a sensitivity-based postprocessing technique were derived and applied to the experimental dataset. In the absence of a turbulence grid and a WG, the turbulence intensity computed with the proposed methodology amounted to $\sim$0.55%. This value was underestimated by $\sim$0.25% due to the neglect of the density fluctuations. In the presence of the turbulence grid, the resulting turbulence intensity was $\sim$2.5%, in fair agreement with the value estimated by a correlation proposed by Roach [17]. In the presence of the grid, if the density fluctuations were neglected, a severe underestimation of the turbulence intensity of $\sim$1% occurred. According to these results, neglecting the contribution of the density fluctuations provided nonnegligible differences. Consequently, the use of a cross-wire probe, coupled with the proposed calibration and postprocessing methodology, was necessary in order to decouple the instantaneous fluctuations of density and velocity and to compute turbulence parameters. The integral length scales were found to be of 12 mm and 17 mm for the tests without and with the turbulence grid, respectively. In the presence of the turbulence grid, the results suggested that the most energetic structures were associated to a length that was in the order of the grid mesh size, amounting to 12 mm.

In order to process the unsteady tests, performed with the WG, two different ensemble-averaging techniques, based on the full rotor revolution and on the single bar passage, were exploited to distinguish the deterministic fluctuations from the background turbulence. The first method allowed the elimination from the spectra of the deterministic frequency components associated both to the bar-passing frequency as well as to the rotor itself, providing thus better results in terms of time-averaged turbulence intensity downstream of the rotor. However, due to the limited number of full rotor revolutions during each test, the statistical convergence was not achieved and the phase-resolved turbulence intensity was poorly measured. If the ensemble-average was performed over a single bar, only the blade passing frequency and its harmonics were eliminated in the spectra, but the phase-resolved turbulence intensity reached the statistical convergence. Finally, if the deterministic noise was not decoupled, the turbulence intensity was overestimated by $\sim$3%.

Acknowledgment

This research is part of the large EU-funded SPLEEN project (Secondary and Leakage Flow Effects in High-SPeed Low-PrEssurE TurbiNes) in collaboration between the von Karman Institute for Fluid Dynamics and Safran Aircraft Engines. The authors thankfully acknowledge the Clean Sky 2 Joint Undertaking for funding of the SPLEEN project (Grant No. 820883) under the European Union's Horizon 2020 research and innovation program. The authors also acknowledge Filippo Biondi, Mariana Lousada, Terence Boeyen, and Oswald Divers for their significant contribution to this work.

Conflict of Interest

There are no conflicts of interest.

Data Availability Statement

The data and information that support the findings of this article are freely available.[3]

[3]https://doi.org/10.5281/zenodo.8075795

Nomenclature

d = wire's diameter (μm)
g = cascade pitch (mm)
k = thermal conductivity (W K^{-1} m^{-1})
l = length (mm)
p = pressure (Pa)
s = blade span (mm)
u = velocity (ms^{-1})
x = location along axial chord (mm)
y = location along pitch direction (mm)
z = location along span direction (mm)
C = blade chord (mm)
N = number (–)
R = resistance (Ω)
S = sensitivity coefficient (–)
T = temperature (K)
E_b = bridge voltage (V)
$K_{1,2,3}$ = parameters of Eq. (13)
$E(f)$ = velocity PSD (dB/Hz)
Tu = turbulence intensity (%)
α = yaw angle (deg)
β = pitch angle (deg)
γ = heat capacity ratio (–)
η = recovery factor (–)
θ = overheat ratio (T_w/T_0) (–)
Λ_{int} = integral length scales (mm)
μ = dynamic viscosity (kg m^{-1} s^{-1})
ρ = density (kg m^{-3})
τ_w = overheating parameter $(T_w - \eta T_0)/(\eta T_0)$ (–)
ϕ = Dewey's corrective factor (–)

Dimensionless Groups

f^+ = reduced wake generator frequency
Kn = Knudsen number
M = Mach number
Nu = Nusselt number
Re = Reynolds number

Abbreviations

BPF = PLA over bar passage
CTA = constant temperature hot-wire anemometry
DPF = PLA over rotor revolution
PLA = phase-locked averaging
PSD = power spectral density
SG = Savitzky–Golay filter
std = standard deviation
SW = single-wire
TG = turbulence grid
WG = wake generator
XW = cross-wire

Superscripts and Subscripts

$(\cdot)'$ = fluctuating component
$\overline{(\cdot)}$ = time-averaged quantity
$\widetilde{(\cdot)}$ = phase-resolved quantity
$(\cdot)_0$ = total flow quantity
$(\cdot)_{1,2}$ = wire 1, wire 2
$(\cdot)_{ax}$ = axial direction
$(\cdot)_b$ = number of blades
$(\cdot)_{class}$ = number of PLA classes
$(\cdot)_{corr}$ = corrected with Dewey's correlation
$(\cdot)_{eff}$ = effective quantity
$(\cdot)_i$ = number of Monte Carlo iterations
$(\cdot)_{in}$ = cascade inlet
$(\cdot)_{out}$ = cascade outlet
$(\cdot)_{per}$ = number of PLA periods
$(\cdot)_s$ = probe support
$(\cdot)_t$ = bridge top resistance
$(\cdot)_{turb}$ = turbulent fluctuations, PLA removed
$(\cdot)_w$ = wire's property
$(\cdot)_{\alpha_0}$ = reference position

References

[1] Bruun, H. H., 1995, *Hot-Wire Anemometry: Principles and Signal Analysis*, Oxford University Press, New York.
[2] Boufidi, E., 2021, "Development of Methods for the Characterization and Uncertainty Assessment of Turbulent Properties in High Speed Compressible Flows, by Hot Wires and Fast Response Pressure Probes," Ph.D. thesis, UCL-Université Catholique de Louvain, Louvain-la-Neuve, Belgium.
[3] Boufidi, E., and Fontaneto, F., 2016, "Towards a More Reliable Application of Hot-Wire Anemometry in Complex Compressible Flows," XXIII Biannual Symposium on Measuring Techniques in Turbomachinery, Transonic and Supersonic Flow in Cascades and Turbomachines, Stuttgart, Germany, Sept. 1–2.
[4] King, L. V., 1914, "XII. On the Convection of Heat From Small Cylinders in a Stream of Fluid: Determination of the Convection Constants of Small Platinum Wires With Applications to Hot-Wire Anemometry," Philos. Trans. R. Soc. London, **214**(509–522), pp. 373–432.
[5] Chemnitz, S., and Niehuis, R., 2020, "A Comparison of Turbulence Levels From Particle Image Velocimetry and Constant Temperature Anemometry Downstream of a Low-Pressure Turbine Cascade at High-Speed Flow Conditions," ASME J. Turbomach., **142**(7), p. 071008.
[6] Cukurel, B., Acarer, S., and Arts, T., 2012, "A Novel Perspective to High-Speed Cross-Hot-Wire Calibration Methodology," Experiments Fluids, **53**(4), pp. 1073–1085.
[7] Boufidi, E., Lavagnoli, S., and Fontaneto, F., 2020, "A Probabilistic Uncertainty Estimation Method for Turbulence Parameters Measured by Hot-Wire Anemometry in Short-Duration Wind Tunnels," ASME J. Eng. Gas. Turbines. Power., **142**(3), p. 031007.
[8] Dewey, C. F., 1965, "A Correlation of Convective Heat Transfer and Recovery Temperature Data for Cylinders in Compressible Flow," Int. J. Heat. Mass. Transfer., **8**(2), pp. 245–252.
[9] Nagabushana, K. A., and Stainback, P. C., 1992, Heat Transfer From Cylinders in Subsonic Slip Flows, NASA-CR-4429 Technical Report, Langley Research Center, Hampton, VA.
[10] Klopfer, G. H., 1974, Constant Temperature Hot Wire Anemometry Data Reduction Procedure. NASA-CR-138899, Technical Report No. FM-74-1, California University, Berkeley, CA.
[11] Kovasznay, L. S. G., 1953, "Turbulence in Supersonic Flow," J. Aeronautical Sci., **20**(10), pp. 657–674.
[12] Morkovin, M. V., 1956, Fluctuations and Hot-Wire Anemometry in Compressible Flows, North Atlantic Treaty Organization advisory Group for Aeronautical Research and Development, AGARDograph, vol. 24, pp 1–102.
[13] de Souza, F., and Tavoularis, S., 2020, "Hot-Wire Response in Compressible Subsonic Flow," AIAA. J., **58**(8), pp. 3332–3338.
[14] Yablochkin, E., and Cukurel, B., 2019, "Selection of Optimal Multi-hotwire Probe in Constant Temperature Anemometry (CTA) for Transonic Flows," Exp. Fluids, **60**(2), p. 27.
[15] Motallebi, F., 1994, "A Review of the Hot-Wire Technique in 2-d Compressible Flows," Prog. Aerosp. Sci., **30**(3), pp. 267–294.
[16] Arts, T., 2013, "Aerodynamic Performance of Two Very High Lift Low Pressure Turbine Airfoils (T106C - T2) At Low Reynolds and High Mach Numbers," 5th European Conference For Aeronautics and Space Sciences (EUCASS), Munich, Germany, July 1–5.
[17] Roach, P. E., 1987, "The Generation of Nearly Isotropic Turbulence by Means of Grids," Int. J. Heat Fluid Flow, **8**(2), pp. 82–92.
[18] Simonassi, L., Lopes, G., Gendebien, S., Torre, A. F. M., Patinios, M., Lavagnoli, S., Zeller, N., and Pintat, L., 2022, "An Experimental Test Case for Transonic Low-Pressure Turbines—Part I: Rig Design, Instrumentation and Experimental Methodology," In Proceedings of the ASME Turbo Expo 2022: Turbomachinery Technical Conference and Exposition, Rotterdam, The Netherlands, June 13–17, p. V10BT30A012.
[19] Xie, F., Li, Y., Wang, X., Wang, Y., Lei, G., and Xing, K., 2018, "Numerical Study on Flow and Heat Transfer Characteristics of Low Pressure Gas in Slip Flow Regime," Int. J. Therm. Sci., **124**(2), pp. 131–145.
[20] Heckmeier, F. M., Hayböck, S., and Breitsamter, C., 2021, "Spatial and Temporal Resolution of a Fast-Response Aerodynamic Pressure Probe in Grid-Generated Turbulence," Exp. Fluids, **62**(2), p. 44.
[21] Michálek, J., Monaldi, M., and Arts, T., 2012, "Aerodynamic Performance of a Very High Lift Low Pressure Turbine Airfoil (T106C) at Low Reynolds and High Mach Number With Effect of Free Stream Turbulence Intensity," ASME J. Turbomach., **134**(6), p. 061009.
[22] Lavagnoli, S., Lopes, G., Simonassi, L., and Torre, A. F. M., 2023, SPLEEN — High Speed Turbine Cascade – Test Case Database, Zenodo.